remote sensing

MDPI

Article

Deformation Pattern Classification of Sea-Crossing Bridge InSAR Time Series Based on a Transfer Learning Framework

Lichen Ren, Chengyin Liu * and Jinping Ou

School of Intelligent Civil and Marine Engineering, Harbin Institution of Technology, Shenzhen 518055, China; 20b954029@stu.hit.edu.cn (L.R.); oujinping@hit.edu.cn (J.O.)
* Correspondence: chengyin.liu@hit.edu.cn

Highlights

What are the main findings?

- An InSAR-based framework is proposed to classify sea-crossing bridge deformation patterns using both synthetic and real data.
- Six representative deformation types are identified and modeled, with ensemble learning improving robustness and probabilistic classification outputs preserving uncertainty information.

What are the implications of the main findings?

- The framework reduces dependence on costly labeled datasets by leveraging synthetic data and transfer learning strategies.
- It enables reliable, automatic identification of deformation patterns in sea-crossing bridges, providing probabilistic insights to support engineering safety and decision making.

Abstract

Interferometric Synthetic Aperture Radar (InSAR) provides unique advantages for sea-crossing bridge monitoring through continuous, large-scale deformation detection. Dividing monitoring data into specific deformation patterns helps establish the connection between bridge deformation and its underlying mechanisms. However, the classification of complex and nonlinear bridge deformations often requires extensive manual labeling work. To achieve automatic classification of deformation patterns with minimal labeled data, this study introduces a transfer learning approach and proposes an InSAR-based method for deformation pattern recognition of cross-sea bridges. At first, deformation time series of the study area are acquired by PS-InSAR, with GNSS results confirming less than 10% error. Then, six types of deformation are identified, including stable, linear, step, piecewise linear, power law, and temperature-related types. Large amounts of simulated data with labels are generated based on these six types. Subsequently, four models—TCN, Transformer, TFT, and ROCKET—are trained using synthetic data and finely adjusted using few real data. Finally, the final classification results are weighted by the classification results of multiple models. Even though confidence and global consistency of each single model are also calculated, the final result is the combined result of a set of multi-type confidences. ROCKET achieved the highest accuracy on simulation data (96.27%) in these four representative models, while ensemble weighting improved robustness on real data. The methodology addresses supervised learning's labeled data requirements through synthetic data generation and ensemble classification, producing probabilistic outputs that preserve uncertainty information rather than deterministic labels. The framework enables automatic classification of sea-crossing bridge deformation patterns with minimal labeled data, iden-

check for updates

Academic Editor: Deodato Tapete

Received: 20 August 2025
Revised: 19 October 2025
Accepted: 25 October 2025
Published: 28 October 2025

Citation: Ren, L.; Liu, C.; Ou, J. Deformation Pattern Classification of Sea-Crossing Bridge InSAR Time Series Based on a Transfer Learning Framework. *Remote Sens.* **2025**, *17*, 3567. https://doi.org/10.3390/rs17213567

Copyright: © 2025 by the authors. Licensee MDPI, Basel, Switzerland. This article is an open access article distributed under the terms and conditions of the Creative Commons Attribution (CC BY) license (https://creativecommons.org/licenses/by/4.0/).

tifying patterns with distinct dominant factors and providing probabilistic information for engineering decision making.

Keywords: sea-crossing bridge; deformation classification; InSAR time series signals; transfer learning; deep learning

1. Introduction

InSAR can provide regular, large-scale ground monitoring. Therefore, it has been widely applied in recent years in geological hazard warning [1], urban ground subsidence monitoring [2], and infrastructure safety assessment [3]. Large-scale ground time series data may reflect specific structural change patterns or the effects of certain influencing factors such as temperature and geological changes on regional areas [4]. Therefore, classifying InSAR data helps interpret the information that data reflects about real geographical environments. Faced with massive amounts of InSAR monitoring data, how we might effectively classify and analyze it to extract meaningful surface change features has become a key issue in current remote sensing data processing [5]. InSAR time series data often contains multiple noise sources such as atmospheric delays, orbital errors, and phase unwrapping errors. These noises are intertwined with actual surface deformation signals, increasing the difficulty of deformation pattern recognition [6]. Among various civil structures, the unique geographical environment and critical function of sea-crossing bridges render them a significant focus of research in the field of structural health monitoring [7]. Except for above problems, sea-crossing bridge deformation data exhibits complex nonlinear trends, including a complex geographic environment, seasonal fluctuations, structural spatial difference, sudden events, superposition of gradual changes, and so on. Traditional linear or simple nonlinear methods cannot cover all complex deformation patterns [8]. Regarding classification methods for ground deformation time series data, because deformation patterns are relatively complex, existing neural network methods require large amounts of labeled data for training. However, pattern annotation of time series data requires considerable time and effort [9]. The labeling process is not only time-consuming and labor-intensive but also prone to errors. Many deep learning applications have been abandoned due to the lack of sufficient labeled data [10]. Traditional machine learning methods strictly assume that the training and testing data must share the same feature space and follow the same distribution, which means that a large-scale dataset must be collected and labeled from scratch for each new task. However, in many real-world applications, the target domain often has few or even no labeled samples, while other related domains may have abundant labeled data [11]. Transfer learning has emerged as an effective paradigm to address this dilemma. By leveraging knowledge from a labeled source or auxiliary domain to assist the learning of a target task, transfer learning can significantly reduce the labeling cost and effort required to build an effective model under a new target distribution [12]. This approach relaxes the strict assumption of independent and identically distributed training data, allowing models to transfer knowledge learned from data-rich domains to data-scarce target domains. Based on the characteristics of transfer learning, using reasonably simulated datasets as labeled data can greatly expand the available annotation resources. Therefore, adopting transfer learning methods can greatly reduce annotation costs.

In order to classify the long-term deformation of the sea-crossing bridge, this article adopts Sentinel-1 satellite images of a bridge as its data source. Bridge deformation data was obtained through interference processing. The observed surface deformation phenomena are divided into six change types: stable, linear, step, piecewise linear, power law, and

temperature-related types. To improve classification accuracy and model generalization ability, transfer learning is introduced to expand the training dataset. Combined with the temporal modeling advantages of deep learning, the applicability of multiple neural network structures in deformation classification is explored. This study comparatively analyzes the performance of four representative models in deformation data classification tasks: Temporal Convolutional Network (TCN) [13,14], Transformer [15], Temporal Fusion Transformer (TFT) [16], and Random Convolutional Kernel Transform (ROCKET) [17]. This achieves automatic classification and recognition of sea-crossing bridge deformation patterns, helping improve the intelligence and automation level of bridge deformation monitoring. The identification of different types of bridge deformation patterns is conducive to the subsequent identification of different environmental loads' influence on deformation, and it can provide early warnings of potential structural risks, so as to improve our ability to manage the safety of bridges.

2. Methods

2.1. Transfer Learning

Transfer learning is the application of knowledge acquired from one or more source tasks to a target task in order to improve the learning performance of the target task [18]. Transfer learning attempts to break the constraint of independent and identically distributed training and testing data, enabling models to generalize to new environments and new tasks. For InSAR data, long revisit cycles increase the uncertainty of persistent scatterers, which in turn reduces the number of reliable measurements and results in typically small data volumes [19]. This limitation prevents InSAR data from fully meeting the big-data requirements of data-driven algorithms. Moreover, classification tasks are usually supervised learning, which requires a large amount of labeled data to train the model. Manual labeling of InSAR deformation time series data is a huge workload and is unreliable because of subjective factors [20,21]. Therefore, by establishing simulated datasets based on bridge deformation classification according to the possible causes and mechanisms of bridge deformation, the scale of training data can be effectively increased [22]. In addition, transfer learning can also improve the generalization ability of models. For these reasons, transfer learning is adopted in this research. It should be noted that the labeled real InSAR observations are employed to fine-tune the pre-trained classification models. Through a layer-wise freezing strategy that keeps the majority of the bottom layers fixed, only the high-level feature representations learned by each model are adapted, which in turn affects the final classification weights assigned to each deformation pattern class.

2.2. Deformation Patterns

InSAR time series data originates from synthetic aperture radar carried by satellites. The radar transmits signals and receives echoes reflected from the ground surface. Signals acquired through this measurement approach generally come from persistent scatterers such as buildings, rocks, and bridges that can maintain scattering characteristics for extended periods and possess high coherence, while water bodies typically have no signal or are considered noise. Therefore, classification of scatterer deformation measured by InSAR should also conform to the deformation trends of main research objects such as surface structures and soil–rock materials on land. Based on this assumption, deformation is analyzed by type. Among these, references [23–25] categorize ground deformation into six basic deformation patterns: stable, linear, step, piecewise linear, power law, and others. Building upon this foundation, considering bridges are temperature-sensitive objects, a temperature-related type is added [26]. The definition of each type is as follows.

(1) Stable: The stable time series reflects the state where the ground surface has not undergone significant displacement changes during the observation period, typically manifesting as a time series with small fluctuations around zero values. Signal variations are mainly caused by observation noise and atmospheric effects. This pattern represents a balanced state of regional tectonic stress.
(2) Linear: The linear deformation pattern manifests as continuous changes in the time series at a stable rate, statistically characterized by a small standard deviation of the first-order difference sequence, reflecting the surface response under continuous uniform external forces. This is commonly observed in slow geological processes. The slope of the linear pattern, which represents the deformation rate, is an important evaluation parameter that can be used to predict long-term deformation trends and assess potential risks.
(3) Step: The deformation characteristic is that when the time series curve exhibits a sudden change at a certain moment, after which it may return to stability or continue deforming at a different rate. This pattern is typically closely related to sudden events, such as seismic displacement and landslide events. Identifying step deformation is of critical significance for early identification of geological hazards and emergency response. The magnitude and occurrence time of the step contain important geological change information.
(4) Piecewise linear: The piecewise linear deformation pattern manifests as transitions between two or more linear deformation phases, reflecting significant but non-sudden changes in external conditions or geological forces. This pattern is commonly observed in phenomena such as ground subsidence or rebound processes caused by groundwater level changes. The timing of deformation rate changes in piecewise linear patterns has important indicative significance for understanding geological environmental changes and the impacts of engineering activities.
(5) Power law: The power law deformation pattern manifests as a nonlinear relationship between displacement and time, typically satisfying a power function form and exhibiting nonlinear decay characteristics. This pattern often indicates that the deformation process is gradually stabilizing and the system is transitioning toward a new equilibrium state. It is commonly observed in phenomena such as creep processes of viscoelastic materials and pore water pressure dissipation during consolidation processes. The numerical characteristic is that the deformation rate gradually decreases over time, with intense changes in the initial stage and gradual stabilization in the later stage. The relationship appears approximately linear in logarithmic coordinates.
(6) Temperature-related: The temperature-related deformation pattern manifests as significant correlation between displacement and temperature changes, typically exhibiting seasonal fluctuations. The amplitude of temperature-related deformation depends on the thermal expansion coefficient and dimensions of structural materials. This pattern reflects the thermal expansion and contraction response of surface materials or structures to temperature changes, primarily observed in artificial facilities sensitive to temperature variations such as metal structures including steel bridges, bridge towers, roads, and railway tracks.

The six categories of time series data variation patterns can describe processes from stable states to various dynamic changes. The deformation pattern classification method based on physical mechanisms combines theoretical foundations with practical application requirements, helping to extract deformation influencing factors and engineering safety indicators from InSAR observation data.

2.3. Classification Models

(1) Temporal Convolutional Networks (TCNs)

The implementation of Temporal Convolutional Networks (TCNs) is based on the innovative integration of causal convolution and dilated convolution [27]. The core approach involves constructing temporal feature extractors through stacked one-dimensional convolutional layers, with each layer employing strict causal padding strategies to ensure unidirectional information flow in time, while introducing exponentially increasing dilation factors that enable the receptive field to expand exponentially with network depth, thereby effectively capturing long-range temporal dependencies under relatively fixed parameter constraints. By adjusting dilation factors and the number of network layers, TCN can control the model's receptive field size to capture temporal patterns at different scales. It exhibits good gradient stability, stable memory usage, and the ability to handle dependencies in extremely long sequences.

(2) Transformer

Transformer is a deep learning model based on the attention mechanism [28]. The core structure of Transformer includes an encoder and a decoder, where each module consists of multiple stacked sub-structures. The encoder is responsible for extracting contextual representations of input sequences, while the decoder generates target sequences based on these representations. Transformer breaks free from the constraints of sequential computation and can process entire input sequences in parallel, thus demonstrating significant advantages in modeling long-range dependencies and improving training efficiency.

(3) Temporal Fusion Transformer (TFT)

Temporal Fusion Transformer (TFT) enhances adaptability to multivariate inputs through variable selection networks, gated residual structures, and explicit temporal control modules, enabling more effective identification of local mutations, state transitions driven by heterogeneous variables, and providing high interpretability [29].

(4) Random Convolutional Kernel Transform (ROCKET)

Random Convolutional Kernel Transform (ROCKET) is a lightweight feature extraction method designed for time series classification tasks [30]. The core idea involves mapping original time series to high-dimensional feature spaces through large-scale random convolutional kernel transforms, followed by fast training and prediction using linear classifiers such as Ridge Regression. It demonstrates good performance in certain small-sample training scenarios.

2.4. Framework

To classify the data acquired by InSAR, the workflow is as shown in Figure 1. Firstly, simulated data is generated according to pre-set possible bridge deformation classification categories, with noise added. To be consistent with the actual data processing workflow, denoising and normalization are performed on the noise-added data. Then models are trained using the processed simulated data. Subsequently, real data undergoes the same denoising and normalization process. Part of the real data is manually labeled and added to the model training process fine adjusting classification feature weights, while other real data is used as test. New simulated data is generated according to the previous workflow as validation. Finally, classification accuracy on the new simulated dataset and confidence results for various types on the real dataset are obtained. The final deformation classification result is determined by the weighted integration of the confidence results of different models.

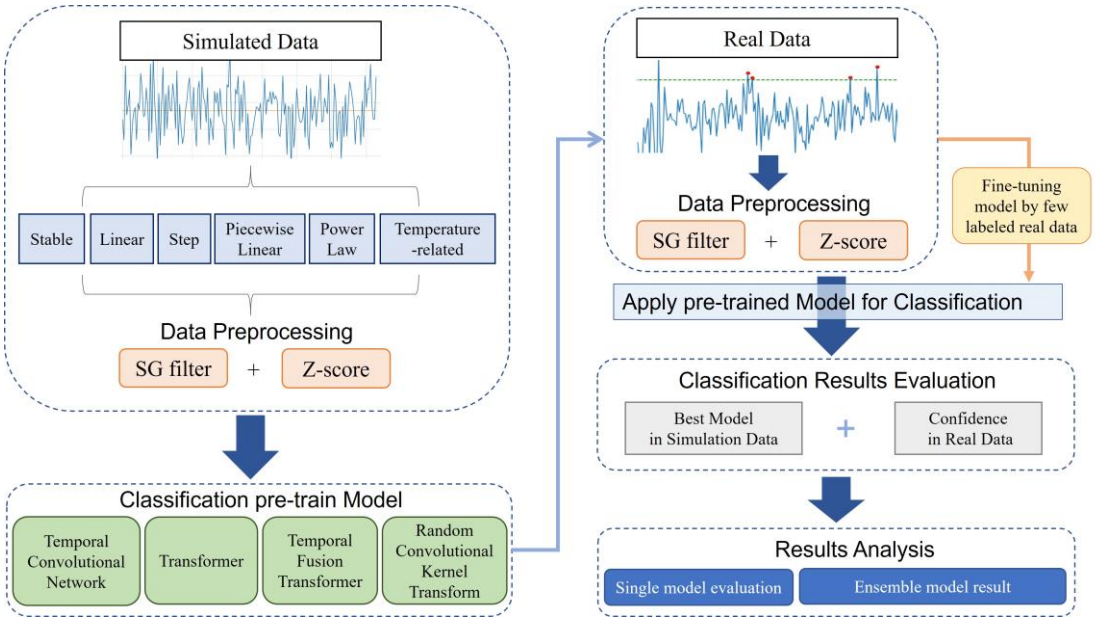


Figure 1. Workflow schematic process.

3. Materials and Results

3.1. Study Area and Dataset

The experimental study area is selected as a sea-crossing bridge, which includes components such as channel bridges, non-navigable span bridges, artificial islands, and undersea tunnels, as shown in Figure 2. The geological conditions of the sea-crossing bridges are complex. Local sections experience uneven settlement due to marine sedimentation and tidal effects. Long-term marine environmental effects impact bridge surface settlement.

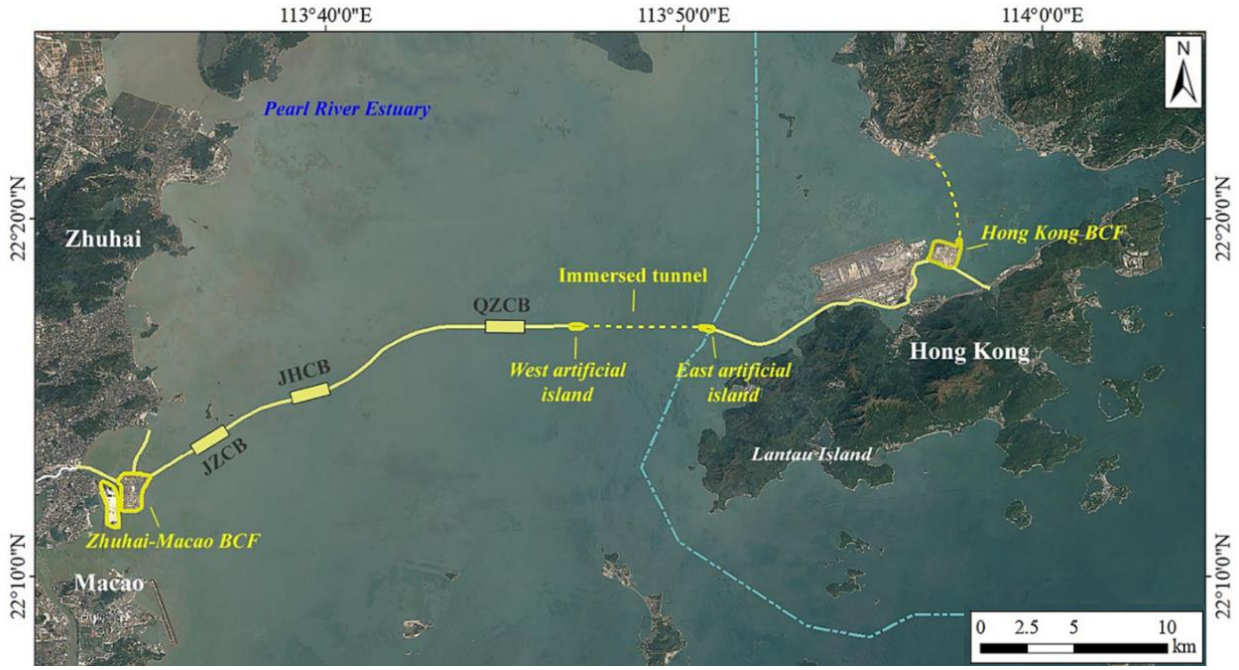


Figure 2. Geographical schematic diagram of the experimental sea-crossing bridge.

The radar satellite images are sourced from the European Space Agency (ESA) Sentinel-1A satellite mission. Its time span covers from 6 January 2018, to 30 December 2023, providing six years of observation period. Sentinel-1A satellite carries C-band Synthetic

Aperture Radar (SAR) sensors. The temporal resolution is 12 days per scene, resulting in a total of 183 SAR images. This study employs Persistent Scatterer Interferometric Synthetic Aperture Radar (PS-InSAR) technology for time series deformation information extraction, with experiment parameters in Table 1 and results in Figure 3. In Table 1, SPS and DPS refer to Single Persistent Scatterer and Distributed Persistent Scatterer, respectively. By selecting persistent scatterer points with stable signals, time-varying atmospheric interference and orbital errors are suppressed. This achieves millimeter-level precision in surface deformation measurements. This study targets the vertical deformation of bridges. With the assumption of negligible horizontal motion, the LOS measurements can be converted to vertical displacements through geometric projection [31,32], and the deformation after that remains vertical unless are special circumstances.

Table 1. Satellite parameters and the parameters set in the experiment.

Item	Value
Satellite	Sentinel-1A
Time span	3 January 2018—30 December 2023
Orbit	Ascending
Satellite orbit	The orbit altitude is 693 km, and the orbit inclination is 98.18°
Revisiting period	12 days
Polarization	VV (Vertical-Vertical polarization)
Wavelength	5.6 cm (C-band)
Resolution	Up to 1 m
Width	Up to 400 km
Acquisition time	Less than 25 min
Geolocation accuracy	About 10 m
Date of master image	2 January 2021
Spatial baseline range	−212.78 m to +136.99 m
Filtering method	Homogeneous Temporal Filter
Amplitude dispersion of SPS	1.2
Mean coherence of SPS	0.5
Sidelobe threshold of SPS	0.35
Amplitude dispersion of DPS	1.5
Mean coherence of DPS	0.3

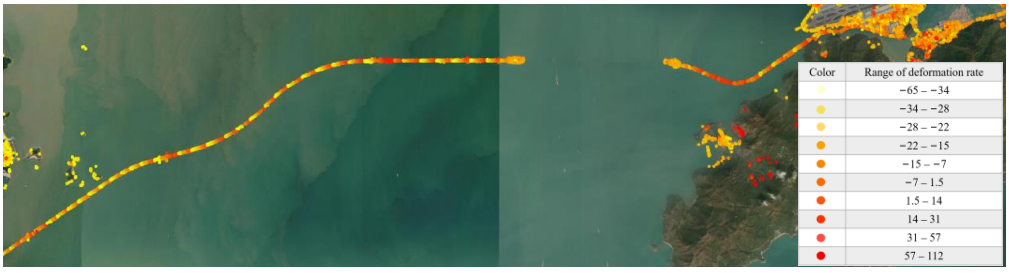


Figure 3. PS-InSAR of the experimental sea-crossing bridge.

To adapt to the data input format of deep learning, the InSAR time series data undergoes preprocessing. The processing workflow includes the following steps: First, data cleaning is performed to remove null values, and supplementing missing values using linear interpolation guarantees a frequency of 12 days. Subsequently, a Savitzky–Golay filter is applied to smooth the original time series signals to reduce noise effects. The filter window length is 7 time points, and the polynomial order is 3. This ensures that the main signal characteristics are preserved while suppressing high-frequency noise. Next, global Z-score standardization is employed. By calculating the mean and standard deviation of the entire dataset, all time series data are remapped to a distribution with mean 0 and standard deviation 1. Normalization eliminates dimensional differences. Finally, the preprocessed data is converted to tensor format. Specific dimensional adjustments are made according to the requirements of different model architectures. This includes adding channel dimensions or reordering sequence order to meet the input requirements of various deep learning models. A total of 1000 real data are selected for manual labeling, which is used to fine-tune the pre-trained model.

3.2. Simulation Dataset

To enhance the similarity between simulated data and real InSAR observations, this study introduces Gaussian white noise into the simulated deformation curves to simulate disturbance components commonly found in interferograms, such as thermal noise, atmospheric delay errors, and radar system errors. By controlling the noise amplitude, the simulated data exhibits a certain degree of random fluctuation based on deformation trends. This approach more closely approximates the statistical characteristics and noise distribution of InSAR data in real scenarios, helping to enhance model robustness and generalization capability.

For transfer learning training, a large-scale simulated InSAR deformation dataset is constructed. This dataset covers six surface deformation types, as shown in Table 2 and Figure 4. These include stable, linear, step, piecewise linear, power law, and temperature-related. Each type generates 10,000 groups of time series data with length n = 183. The simulated time span covers six years. The time series is $\{t_i\}_{i=1}^{n}$, among which $t_i = i$ and n = 183. The final simulation time series is $\widetilde{X}(t) = X(t) + \varepsilon(t)$. All simulated data has independent and identically distributed Gaussian white noise added as $\varepsilon(t) \sim N(0, \sigma^2)$, σ = 0.83, which represents InSAR common coherence noise with reference to [24].

Table 2. Deformation types and analytical expressions.

Label	Deformation Type	Description
0	Stable	Small fluctuations around a constant value, simulating reference points or stable areas.
	$X(t) = c,\ c \sim \mathcal{U}(-2.5, 2.5)$	
1	Linear	Linear upward or downward trends, simulating continuous subsidence or uplift.
	$X(t) = k \cdot \frac{t}{n} \cdot 12,\ k \sim \begin{cases} \mathcal{U}(-3, -0.05),\ downward,\ \text{possiblity} = 0.6 \\ \mathcal{U}(0.5, 2.5),\ upward, \text{possiblity} = 0.4 \end{cases}$	
2	Step	Experiencing a significant sudden change at a certain moment.
	$X(t) = \begin{cases} k_1 \cdot \frac{t}{n} \cdot 12, & t < t_s \\ X(t_s^-) + \Delta + k_2 \cdot \frac{t - t_s}{n} \cdot 12, & t \geq t_s \end{cases}$	

Table 2. *Cont.*

Label	Deformation Type	Description
3	Piecewise linear	Containing multiple phases of subsidence or recovery trends.
	$X(t) = \begin{cases} k_1 \cdot \frac{t}{n} \cdot 12, & t < t_1 \\ X(t_1^-) + k_2 \cdot \frac{t-t_1}{n} \cdot 12, & t_1 \le t < t_2 \\ X(t_2^-) + k_3 \cdot \frac{t-t_2}{n} \cdot 12, & t \ge t_2 \end{cases}$	
4	Power law	Nonlinear trends, simulating landslide or post-earthquake deformation recovery processes.
	$X(\tau) = \begin{cases} -s \cdot \alpha \cdot \tau^{\beta}, & \textit{decelerating deformation} \\ +s \cdot \alpha \cdot [1-(1-\tau)^{\beta}], & \textit{accelerating deformation} \end{cases}$	
5	Temperature-related	Exhibiting certain correlation with temperature sequences, simulating components or areas significantly affected by temperature.
	$X(t) = a \cdot Z(t) + b$ $Z(t) = \frac{T(t)-\mu_T}{\sigma_T} \cdot 5$ is a standardized temperature sequence, and $a \in [0.3, 0.8]$, $b \in [-3, 3]$ are random fitted parameters. $T(t)$, the temperature data, is sourced from actual temperature station measurements. This study uses atmospheric temperature data from a temperature station located at longitude 22.2831° and latitude 113.7311°.	

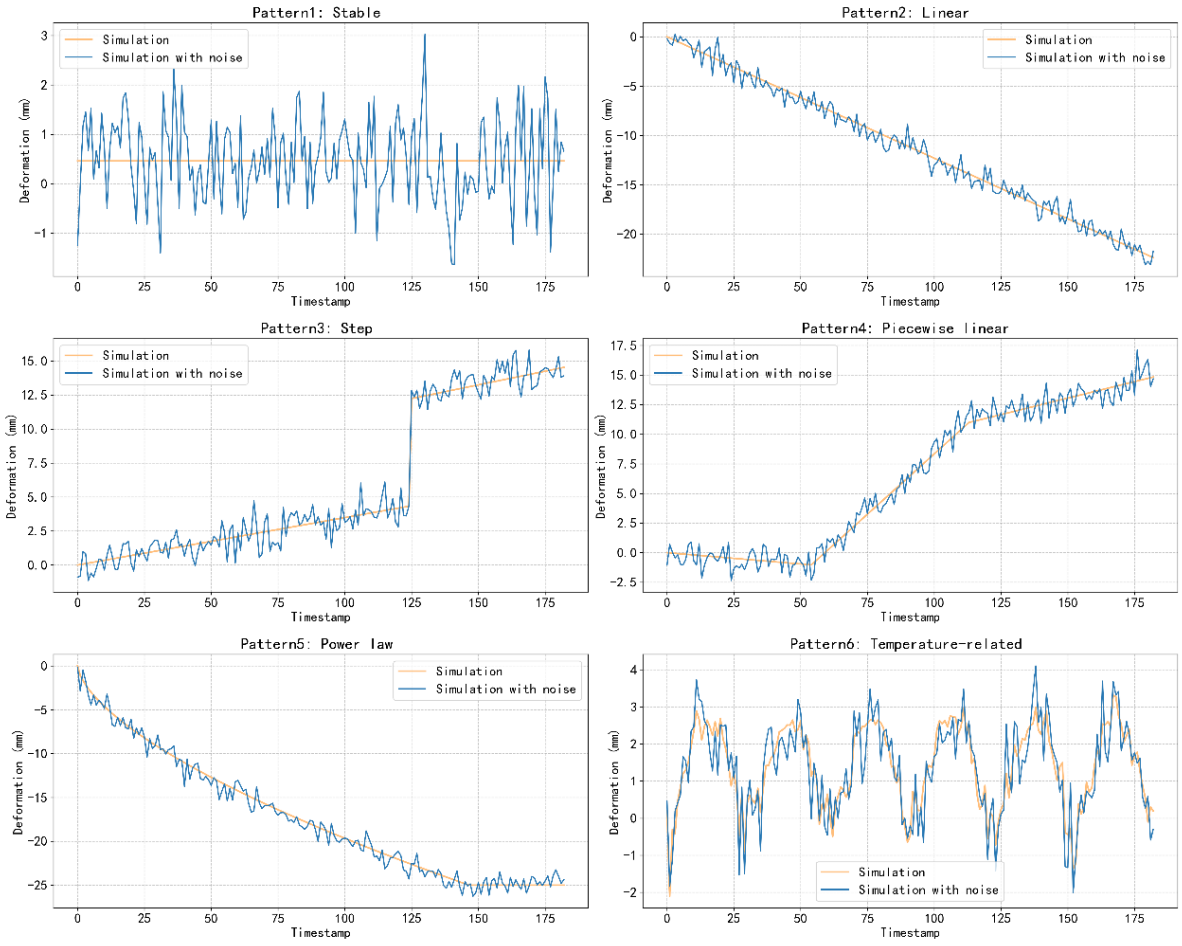


Figure 4. Simulation data samples.

During model training, after pretraining with a simulated dataset, a small amount of manually labeled measured data is added for fine-tuning.

3.3. Training Process of the Model

The specific experimental workflow consists of the following steps. First, a simulated dataset was established according to Section 3.2 for model training, and the actual bridge monitoring data was processed using PS-InSAR technology. Next, the time series data underwent preprocessing through Savitzky–Golay filtering and Z-score normalization. Subsequently, TCN, Transformer, ROCKET, and TFT deep learning models were trained in parallel, employing an 80/20 training–validation split and early stopping mechanism to optimize the training process. After training completion, each model was fine-tuned using a small amount of labeled real data, with most lower layers frozen and only the top layer weights adjusted. The models then generated deformation classification results and confidence matrices. The temporal Consistency Score (TCS) and Global Class Consistency Score (GCS) were calculated. During the training process of each model, a meta-learner was established to record model parameters and learned features. The meta-learner dynamically learned the weight variations based on the confidence results from each model's classification outputs, thereby integrating the ensemble model. The present study employs several classification models that underwent a pre-training process with specific parameter configurations tailored to our dataset. These hyperparameters have demonstrated robust performance in previous bridge monitoring experiments, providing preliminary evidence for their suitability in similar time series classification tasks for structural health monitoring applications. The values of some hyperparameters are shown in Table 3.

Table 3. Hyperparameters of each model.

Model	Hyperparameters
TCN	Kernel size: 3 Dropout: 0.3
Transformer	Hidden dimension: 128 Number of attention heads: 8 Number of encoder layers: 3 Dropout: 0.1
TFT	Hidden size: 128 Number of attention heads: 4 Number of transformer layers: 2
ROCKET	Number of kernels: 2000

3.4. Model Evaluation Index

To systematically evaluate the performance of different temporal models in InSAR deformation classification tasks, this study designs a complete experimental workflow including data division, training optimization, performance evaluation, and model selection. The simulated dataset is divided into training and validation sets at an 8:2 ratio, with each surface deformation sample maintaining consistent class distribution across the two subsets. To compare the performance of multiple models on real observational data, this paper uses confidence scores and temporal consistency scores.

Confidence is used to measure the degree of certainty of the model's prediction results. Higher confidence indicates that the model is more certain that the sample belongs to the predicted category. For each sample i, the class probability output by the model is a vector $P_i = [p_{i1}, p_{i2}, \ldots, p_{iC}]$, and C is the number of categories. Confidence is defined as the

maximum probability value: $Confidence = \max_{c \in \{1,\ldots,c\}} p_{ic}$. The overall confidence score is the mean of all samples: $Confidence\ score = \frac{1}{N}\sum_{i=1}^{N} \max_{c} p_{ic}$.

Temporal consistency measures the consistency between predicted categories and their time series change patterns. The calculation is based on the correspondence between typical patterns of each deformation type and the time series curves. It is calculated only for categories with structurally distinguishable temporal characteristics (i.e., change categories with labels 0, 1, 2, 3). We define a set of typical feature detection functions $f_c(x_i)$ and determine whether the time series of the i-th sample x_i conforms to the typical characteristics of its predicted category:

$$\mathrm{TC}_i = \begin{cases} 1, & \text{if } f_{y_i}(\mathbf{x}_i) = \text{True} \\ 0, & \text{otherwise} \end{cases}$$

Therefore, temporal consistency is $\mathrm{TCS} = \frac{1}{\sum_{i=1}^{N} \mathbb{I}(y_i \in \{0,1,2,3\})} \sum_{i=1}^{N} \mathrm{TC}_i$

In addition, to provide a reference for evaluating the accuracy of each model, global consistency scores (GCSs) are added to evaluate the classification accuracy of different models on different simulated datasets. The global consistency score calculates the proportion of agreement between model-predicted types and true types. The trained models are applied to classify simulated datasets that differ from the training data. Since this simulated dataset has labels, the generalization ability of the model can be assessed by examining the deviation between predicted classification labels and actual labels.

3.5. Result

(i) Performance evaluation on real data

Since deformation patterns are not single deformation trends such as linear or power law changes, they are usually mixed by multiple patterns. Confidence can only indicate which category each model tends to classify a time series dataset into during classification. Due to the complexity of actual geographical changes and them being influenced by multiple factors, it is impractical to definitively classify InSAR time series data into a specific category. According to confidence levels, this time series dataset is classified by what change trends compose it, with an example shown in Figure 5.

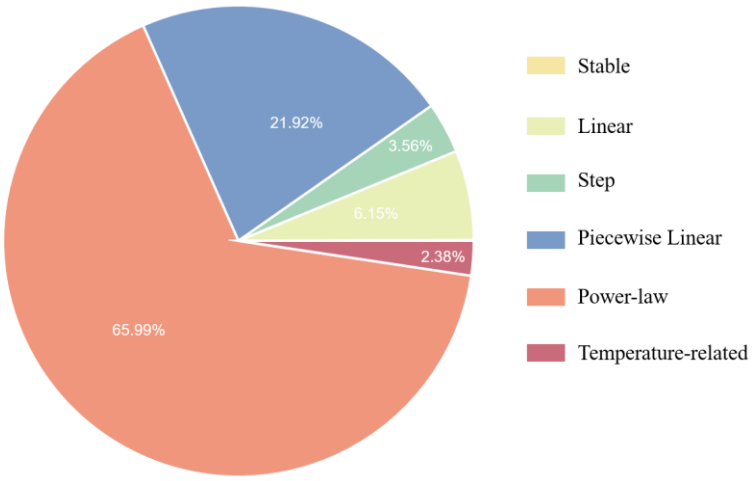


Figure 5. Example of confidence level for time series data classification.

For different categories combined with specific geographical features, attention is focused on different trend information. For example, for landslides, attention is paid to step-type change points or whether power law trends are establishing a new equilibrium. Figure 6 shows the confidence values of the categories with the highest confidence during classification. Most values exceed 0.5, indicating that for most time series data, there exists a change pattern that accounts for more than 50% of the proportion, capable of reflecting the majority of the change trends in this time series data.

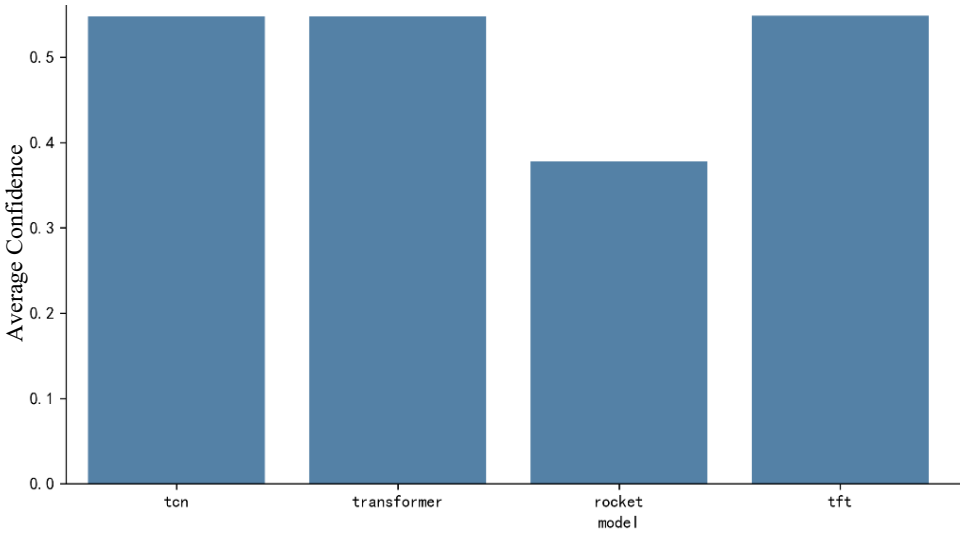


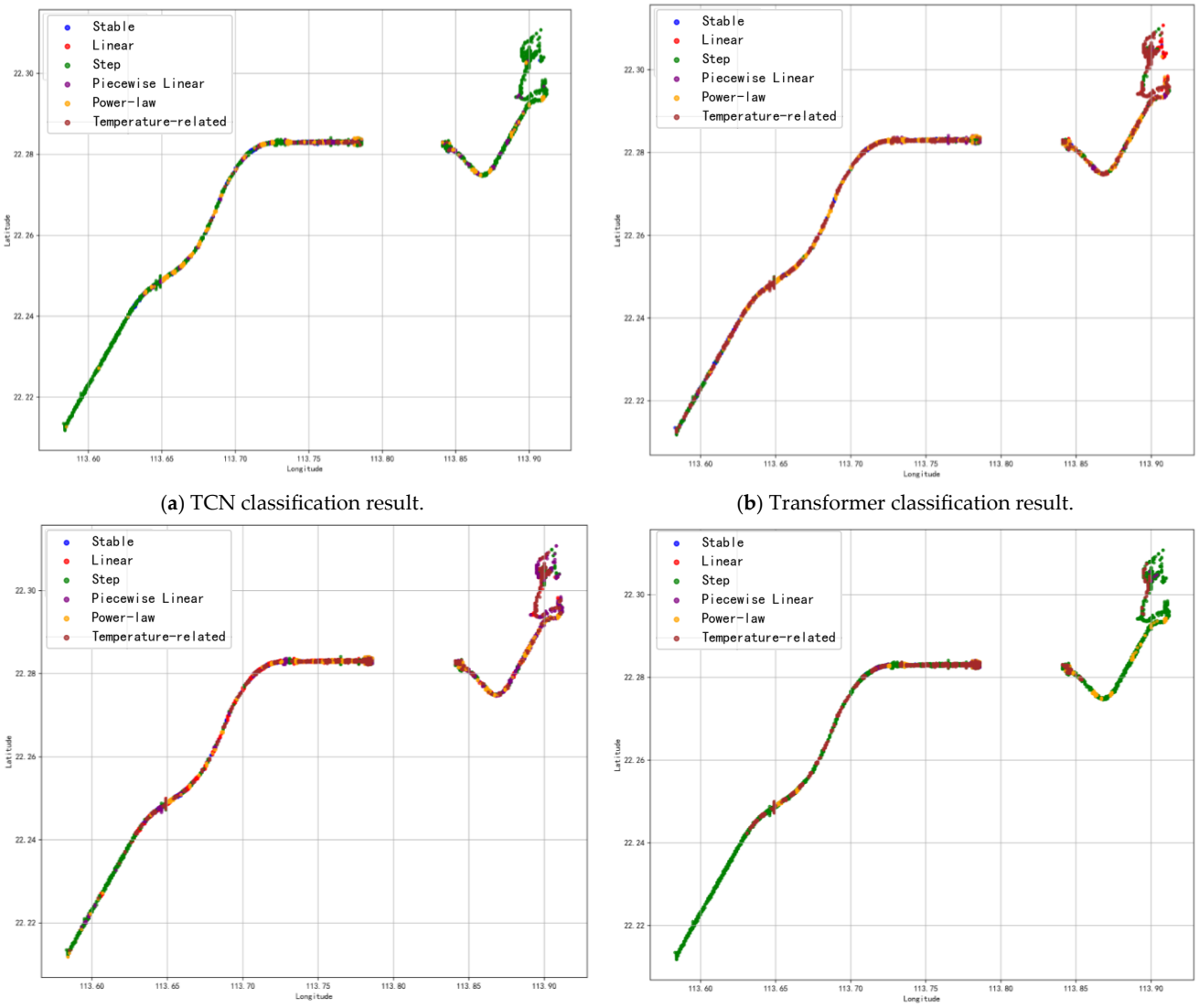
Figure 6. Average classification confidence of each model.

According to Figure 7, the classification results of different models vary significantly in some regions. TCN identifies more of the data from these areas in which slope undergoes sudden changes as step type, while other algorithms identify them as piecewise linear or temperature-related type. The difference between step and piecewise linear is that step type returns to the pre-change trend after the sudden change occurs, while piecewise linear transitions to a different linear trend after the change. In actual InSAR data, these two patterns often have transition zones, and different models have different sensitivities to these transition zones. For practical engineering applications, the focus is often on the location of the mutation points. Therefore, to some extent, this reflects the same trend, namely the time and geographical location where sudden changes may occur.

ROCKET has the shortest runtime and performs best on the original simulated dataset, with fewer parameters to adjust. Ensemble models like TFT may not be suitable for small samples. Although Transformer does not perform well on the simulated dataset, it can display process information from classification prediction according to the attention mechanism. Therefore, in the task of classification by single model, ROCKET performs better among the four.

(ii) Similarity of classification results of different models

Looking at Figure 7, it is not straightforward to estimate the similarity between the classification results of each model. Since the actual maximum confidence is usually between 50% and 60%, it is easy for each model to produce different results by looking only at the highest confidence type. Therefore, similarity verification of the models' classification results is carried out, and the results are shown in Figure 8. This indirectly demonstrates the reliability of the classification results, with differences arising from each model's varying ability to capture different patterns in the data. Therefore, by integrating the feature representations from each model through an adaptive fusion mechanism, the final classification achieves greater reliability and robustness.



(**a**) TCN classification result.

(**b**) Transformer classification result.

(**c**) TFT classification result.

(**d**) ROCKET classification result.

Figure 7. The classification results schematic diagram of experimental sea-crossing bridge for each model (selecting the classification result corresponding to the maximum confidence level).

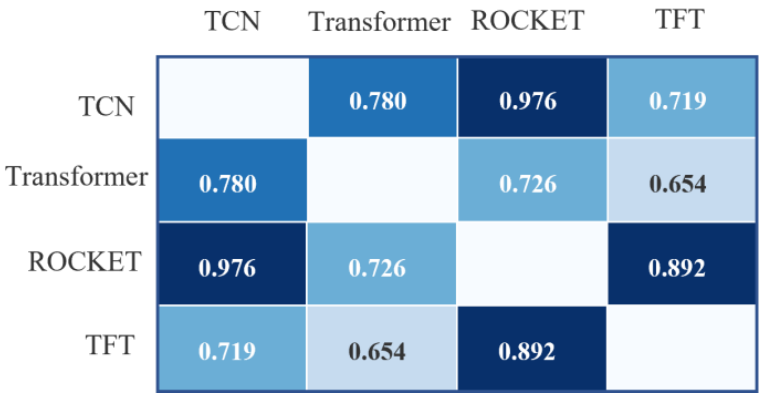


Figure 8. Model similarity heatmap.

(iii) Performance evaluation on simulation data

Since real data largely does not have labels, the classification results on real data cannot demonstrate the classification accuracy of each model. Therefore, trained models are used to classify another set of simulated data with different random parameters that differ from those of the training data. By validating the accuracy of classification results, the generalization ability of the models is reflected to a certain extent, which is referred to as the GCS. The GCS results are shown in Table 4. The GCS confirms ROCKET's superior accuracy (96.27%), outperforming TCN (70.3%), Transformer (77.4%), and TFT (64.7%).

Table 4. Global consistency score of each model.

Model	GCS
TCN	0.7028
Transformer	0.7742
TFT	0.6470
ROCKET	0.9627

It is clearly evident that on different simulated datasets, ROCKET achieves better classification performance with the shortest runtime and requires the fewest parameters to adjust.

4. Discussion

4.1. Classification Results Based on Weight and Spatiality

Different classification algorithms exhibit significant differences in bridge deformation identification processes, which are mainly due to three reasons. First, the sensitivity and weight allocation strategies for input feature parameters vary fundamentally among algorithms, leading to inconsistent importance evaluations of the same features across different models. Second, the decision boundaries constructed by various algorithms in high-dimensional feature spaces present different geometric characteristics and complexity levels, resulting in divergent classification judgments for boundary samples. Finally, the distribution characteristics of training samples affect the learning effectiveness and generalization capabilities of different algorithms to varying degrees, further intensifying the uncertainty of classification results.

Considering the inherent differences and complementarity among the aforementioned algorithms, this study employs a deep feature fusion strategy to construct the ensemble model. Unlike traditional weighted voting or decision-level fusion methods, this strategy concatenates the intermediate-layer feature representations of four heterogeneous models—TCN, Transformer, ROCKET, and TFT—and introduces a learnable fusion network to adaptively integrate multi-source features. Specifically, each base learner independently extracts discriminative feature vectors, and the fusion layer adopts a multi-layer perceptron (MLP) structure to perform nonlinear transformation and dimensionality reduction on the concatenated high-dimensional features, learning the optimal feature combination method. This feature-level fusion strategy can fully utilize the complementary advantages of each algorithm at the feature extraction level, preserve richer intermediate-layer information, and has stronger expressive power and generalization performance compared to simple voting or averaging methods, thus obtaining more robust and reliable classification results. The final classification results of bridge deformation are shown in Figure 9.

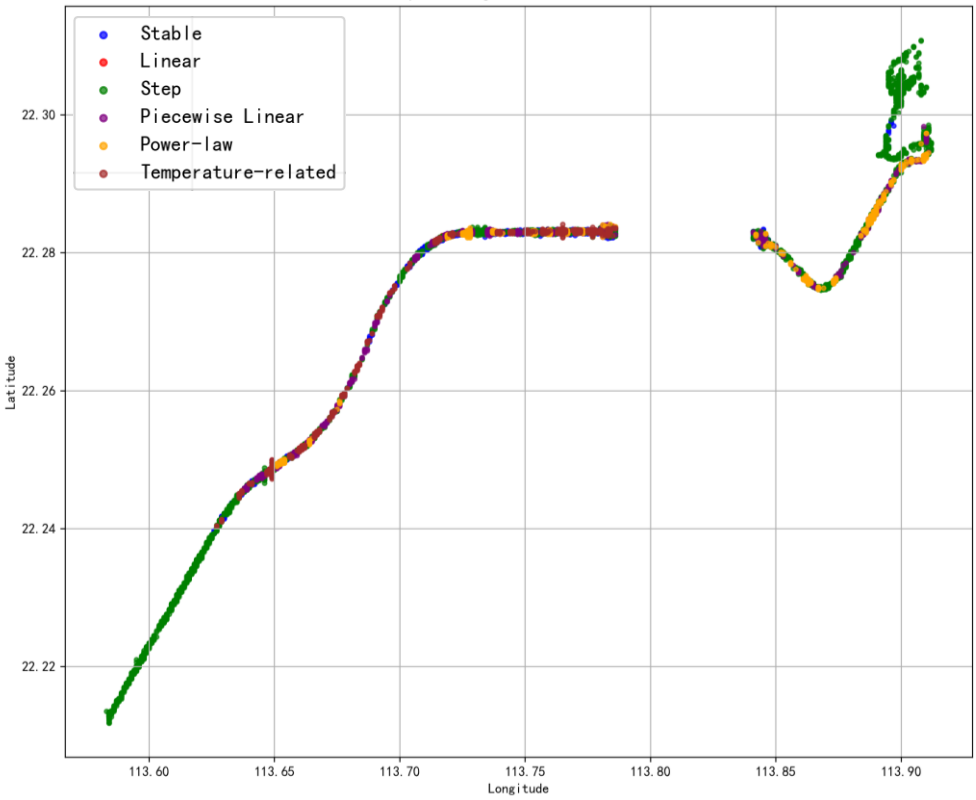
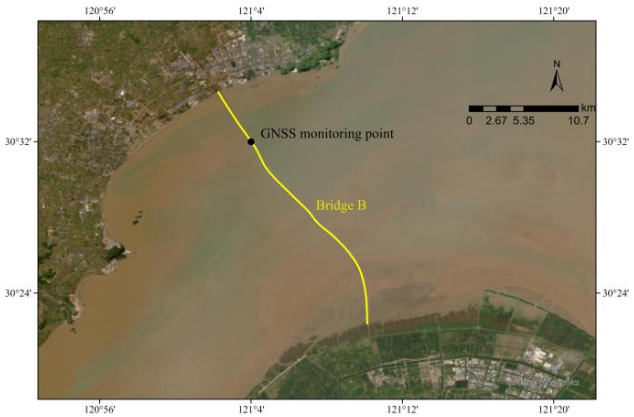


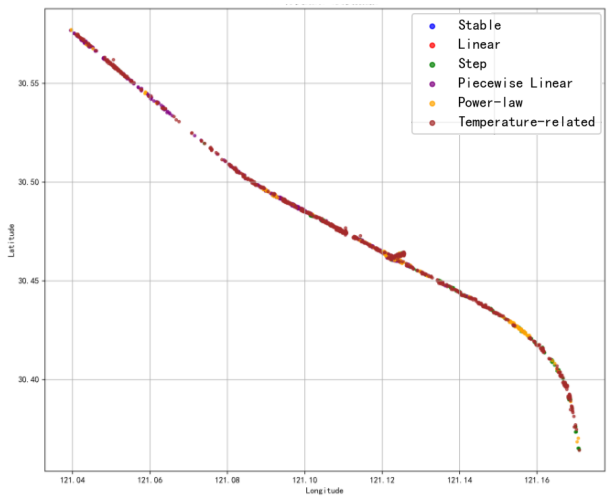
Figure 9. Classification results weighted by multiple models.

4.2. Generalization Capability of the Method

To demonstrate the classification generalization capability, the model is applied to another sea-crossing bridge, bridge B. Research data are also sourced from the Sentinel-1A satellite, with a timeline of December 2015 to October 2023. It is worth noting that this bridge has GNSS monitoring point G in Figure 10. Comparing the deformation monitoring results of GNSS and InSAR, the difference is within 10 percent, indicating the reliability of the InSAR monitoring data. The InSAR monitoring showed that the settlement value of 2023 was 3.6 mm, while the GNSS monitoring indicated a settlement value of 4 mm. The remaining data process flow is the same as in Section 3. Finally, the classification results of bridge B are obtained and shown in Figure 10.

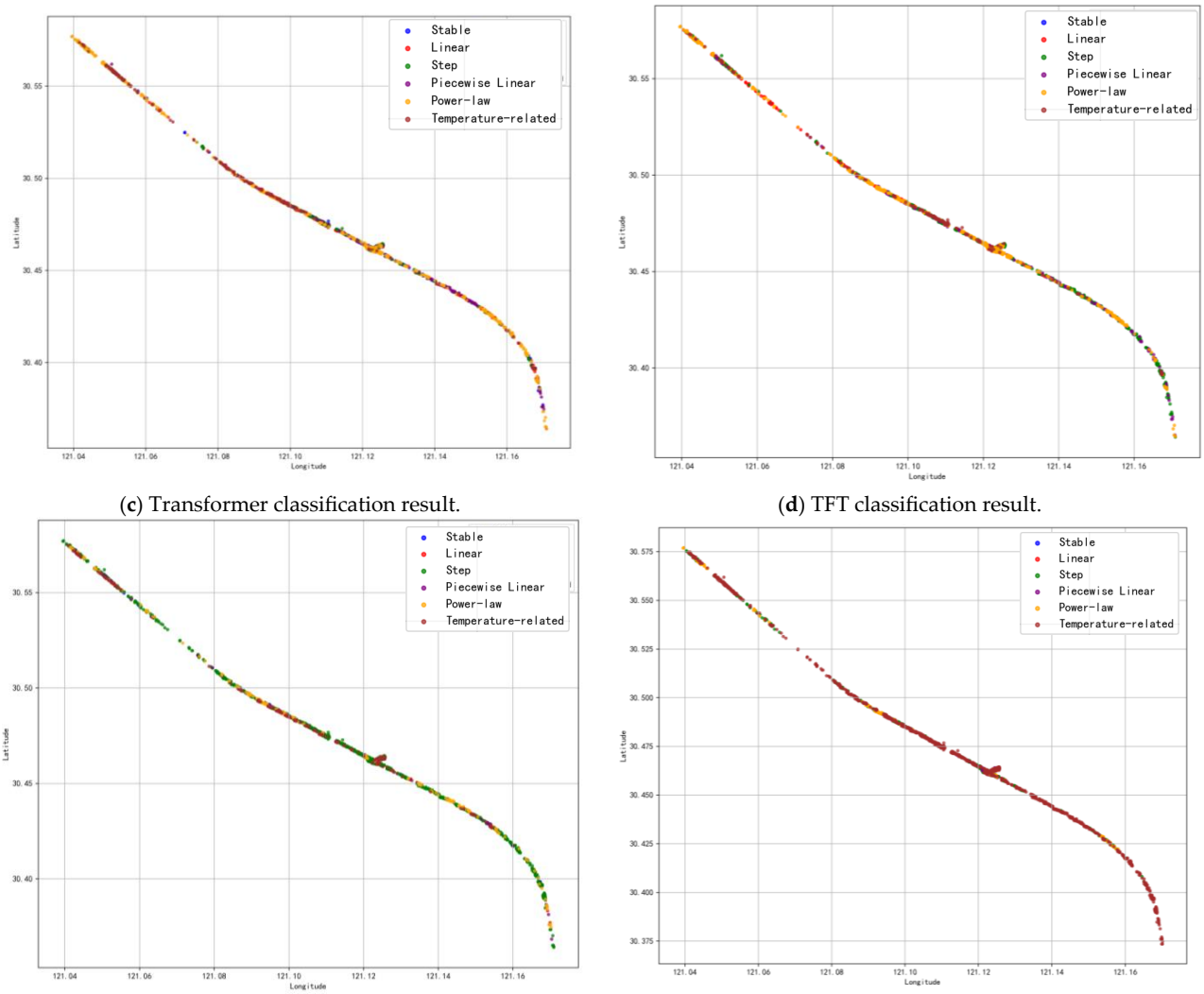


(**a**) The geographical location of bridge B.



(**b**) TCN classification result.

Figure 10. *Cont.*



(**c**) Transformer classification result.

(**d**) TFT classification result.

(**e**) ROCKET classification result.

(**f**) Classification results weighted by multiple models.

Figure 10. The classification results schematic diagram of Bridge B for each model (selecting the classification result corresponding to the maximum confidence level).

It can be seen that, similar to the sea-crossing bridge in the experiment, the displacements of most points on the bridge are the temperature-related type, followed by the piecewise linear type. The long-term classification results can provide experience feedback for bridge design and transformation and provide a scientific basis for service performance evaluation and reinforcement decision making in relation to sea-crossing bridges.

4.3. Deformation Types in Cable-Stayed Bridges

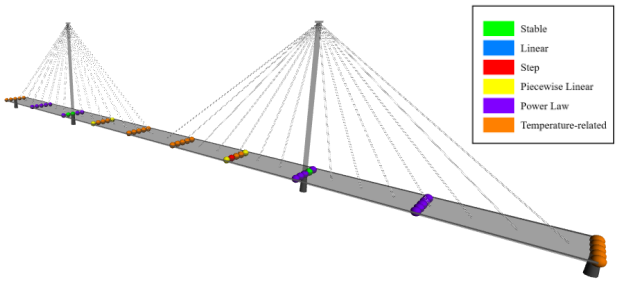
Sometimes, for large sea-crossing bridges, more attention is paid to statically indeterminate structures, which mainly include navigation channel bridges. The classification results of a cable-stayed bridge A1 (one cable-stayed bridge in the study area in Section 3.1) and Bridge B1 (one cable-stayed bridge, i.e., Bridge B in Section 4.2) are shown as Figure 11, where the mid-span is the mainly temperature-related type, while the areas near the bridge towers are predominantly the power law type. Bridge B1 has fewer permanent scatterers. It can also be proven that the number of permanent monitoring scatterers is unstable.



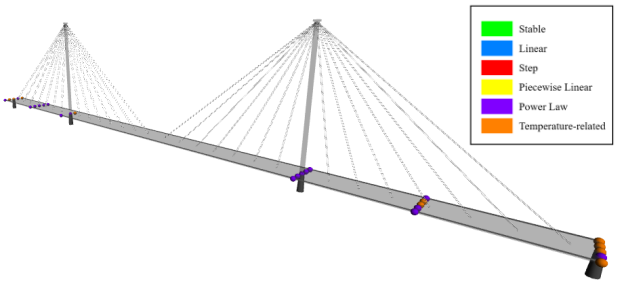
(**a**) Bridge A1.



(**b**) Bridge B1.



(**c**) Classification result of cable-stayed bridge A1.



(**d**) Classification result of cable-stayed bridge B1.

Figure 11. Classification result of cable-stayed bridge A1 and bridge B1.

The classification results of long-term InSAR monitoring data can reflect the stress characteristics and adaptability of different structural parts. Meanwhile, the classification may also correspond to the effect of different external factors such as temperature effect, foundation settlement, wind, and wave load. For statically indeterminate structures such as cable-stayed bridges, the more dangerous situation is uneven settlement and abrupt change. Sudden uneven settlement can lead to a subsequent increase in bridge internal force and long-term development can lead to fatigue damage and other problems. Some bridge settlement mutation may also reveal early disease; for example, the step type appears, and the value changes greatly. Different types of deformation patterns are identified to provide early warning for potential structural risks, so as to improve the safety management level of bridges.

5. Conclusions

This study is an attempt to apply InSAR measurement results to identify sea-crossing bridge deformation patterns. Based on the PS-InSAR measurement results, time series data is divided into six main types according to the long-term influencing factors that may affect bridge deformation. Using transfer learning methods, reasonable simulated data and partially labeled real data are used to expand the training dataset. This effectively overcomes the insufficient volume of InSAR experimental data. Subsequently, multiple data-driven algorithms are combined to complete the classification process of deformation time series data. Finally, the final classification result is obtained by fusing the features from various methods through a learnable fusion network. This method can utilize more datasets and multi-type approaches to capture the characteristics of deformation time series data. It provides a basis for understanding the physical significance behind bridge deformation reflected by InSAR time series. Based on the research, the following conclusions are obtained:

(1) Long-term bridge deformation time series can be classified as stable, linear, step, piecewise linear, power law, and temperature-related types. However, actual sea-

crossing bridge deformation is a mixture of these six types. Although there may sometimes be a major component type with a larger proportion, it is necessary to analyze all displacement types that constitute the major proportions to obtain more complete results.

(2) Transfer learning can use simulated data to expand the training data of classification models and improve the generalization ability of models. Experimental data is trained on several models including TCN, Transformer, TFT, and ROCKET. ROCKET achieves the fastest speed and highest accuracy, with 96.27% accuracy in different simulated datasets and the fewest parameters to adjust. Among these models, it can be considered the most suitable model for this task.

(3) Most of the long-term deformation of sea-crossing bridges exhibits complex nonlinear time series characteristics, making it difficult to simply categorize into a single class. Therefore, a better classification approach should provide a combination of multiple types with confidence values. By fusing the intermediate feature representations of each model rather than simply combining their final decisions, the system can retain more discriminative information and learn optimal feature combinations through a learnable fusion network. This feature-level fusion strategy preserves richer information compared to decision-level methods, providing more comprehensive insights for engineering decision-making.

This study reveals the inherent patterns of different algorithms in classification performance, uncertainty manifestation, and engineering applicability through in-depth comparative analysis of multiple machine learning methods in bridge deformation classification. Due to the complexity of real ground deformation data, the similarity between current simulated data and real data still needs improvement. However, current classification methods can provide reference for automatic identification and causal analysis of InSAR data. Future research will integrate additional data sources (e.g., GNSS networks, temperature sensors) and explore multi-sensor fusion to further improve deformation pattern recognition for intelligent bridge monitoring. By combining data analysis and physical mechanisms and focusing on the engineering interpretation, the monitoring results can serve the bridge's operation, maintenance, and management.

Author Contributions: Conceptualization, C.L. and J.O.; methodology, C.L. and L.R.; software, L.R.; validation, C.L. and L.R.; formal analysis, L.R.; investigation, L.R.; resources, C.L.; data curation, L.R.; writing—original draft preparation, L.R.; writing—review and editing, C.L.; visualization, L.R.; supervision, C.L.; project administration, C.L.; funding acquisition, J.O. All authors have read and agreed to the published version of the manuscript.

Funding: This research was funded by the National Key Research and Development Program of China (Grant No. 2022YFB2602102), the National Natural Science Foundation of China (Grant No. 52378295), the Natural Science Foundation of Guangdong Province (Grant No. 2024A1515010296), the Guangdong Provincial Key Laboratory of Intelligent and Resilient Structures for Civil Engineering (Grant No. 2023B1212010004), and the Shenzhen S&T Project (Grant Nos. KQTD20210811090112003, KJZD20231023093057005 and KCXFZ20240903094301003). The authors are grateful to the authorities for their support.

Data Availability Statement: The original data presented in the study are openly available from the Copernicus Open Access Hub (https://copernicus.eu/) and the Alaska Satellite Facility (ASF) Data Search (https://search.asf.alaska.edu/).

Conflicts of Interest: The authors declare no conflict of interest.

References

1. Fontana, M.; Bernardi, M.S.; Cigna, F.; Tapete, D.; Menafoglio, A.; Vantini, S. Identification of Precursors in InSAR Time Series Using Functional Data Analysis Post-Processing: Demonstration on Mud Volcano Eruptions. *Remote Sens.* **2024**, *16*, 1191. [CrossRef]
2. Liu, S.; Bai, M. Spatiotemporal Characteristics of Ground Subsidence in Xiong'an New Area Revealed by a Combined Observation Framework Based on InSAR and GNSS Techniques. *Remote Sens.* **2025**, *17*, 2654. [CrossRef]
3. Xie, L.; Liu, J.; Wang, X.; Wu, S.; Ali, E.; Xu, W. Decadal and Heterogeneous Deformation of Breakwater Dams and Reclaimed Lands in Xuwei Port Revealed by Radar Interferometry Measurements. *Remote Sens.* **2025**, *17*, 2778. [CrossRef]
4. Zhang, K.; Wang, Y.; Zhao, F.; Ma, Z.; Zou, G.; Wang, T.; Zhang, N.; Huo, W.; Diao, X.; Zhou, D.; et al. An Underground Goaf Locating Framework Based on D-InSAR with Three Different Prior Geological Information Conditions. *Remote Sens.* **2025**, *17*, 2714. [CrossRef]
5. Barra, A.; Solari, L.; Béjar-Pizarro, M.; Monserrat, O.; Bianchini, S.; Herrera, G.; Crosetto, M.; Sarro, R.; González-Alonso, E.; Mateos, R.M.; et al. A Methodology to Detect and Update Active Deformation Areas Based on Sentinel-1 SAR Images. *Remote Sens.* **2017**, *9*, 1002. [CrossRef]
6. Ma, P.; Lin, H. Robust detection of single and double persistent scatterers in urban built environments. *IEEE Trans. Geosci. Remote Sens.* **2015**, *54*, 2124–2139. [CrossRef]
7. Jiang, Y.; Guo, C.; Wang, J.; Xu, R. Multipath Effects Mitigatin in Offshore Construction Platform GNSS-RTK Displacement Monitoring Using Parametric Temporal Convolution Network. *Remote Sens.* **2025**, *17*, 601. [CrossRef]
8. Talledo, D.A.; Miano, A.; Bonano, M.; Di Carlo, F.; Lanari, R.; Manunta, M.; Meda, A.; Mele, A.; Prota, A.; Saetta, A.; et al. Satellite radar interferometry: Potential and limitations for structural assessment and monitoring. *J. Build. Eng.* **2022**, *46*, 103756. [CrossRef]
9. Bai, S.; Kolter, J.Z.; Koltun, V. An empirical evaluation of generic convolutional and recurrent networks for sequence modeling. *arXiv* **2018**, arXiv:1803.01271. [CrossRef]
10. Pan, S.J.; Qiang, Y. A Survey on Transfer Learning. *IEEE Trans. Knowl. Data Eng.* **2010**, *22*, 1345–1359. [CrossRef]
11. Weiss, K.; Khoshgoftaar, T.M.; Wang, D. A survey of transfer learning. *J. Big Data* **2016**, *3*, 9. [CrossRef]
12. Alzubaidi, L.; Bai, J.; Al-Sabaawi, A.; Santamaría, J.; Albahri, A.S.; Al-Dabbagh, B.S.N.; Fadhel, M.A.; Manoufali, M.; Zhang, J.; Al-Timemy, A.H.; et al. A survey on deep learning tools dealing with data scarcity: Definitions, challenges, solutions, tips, and applications. *J. Big Data* **2023**, *10*, 46. [CrossRef]
13. Liu, C.; He, Y.; Zhang, X.; Wang, Y.; Dong, Z.; Hong, H. CS-FSDet: A Few-Shot SAR Target Detection Method for Cross-Sensor Scenarios. *Remote Sens.* **2025**, *17*, 2841. [CrossRef]
14. Luo, W.; Dou, J.; Fu, Y.; Wang, X.; He, Y.; Ma, H.; Wang, R.; Xing, K. A Novel Hybrid LMD–ETS–TCN Approach for Predicting Landslide Displacement Based on GPS Time Series Analysis. *Remote Sens.* **2023**, *15*, 229. [CrossRef]
15. Zhang, D.; Ma, W.; Jiao, L.; Liu, X.; Yang, Y.; Liu, F. Multiple Hierarchical Cross-Scale Transformer for Remote Sensing Scene Classification. *Remote Sens.* **2025**, *17*, 42. [CrossRef]
16. Moualla, L.; Rucci, A.; Naletto, G.; Anantrasirichai, N.; Da Deppo, V. Hybrid GIS-Transformer Approach for Forecasting Sentinel-1 Displacement Time Series. *Remote Sens.* **2025**, *17*, 2382. [CrossRef]
17. Ou, Y.; Wei, Y.; Rodríguez-Aldama, R.; Zhang, F. A Lightweight Deep Learning Model for Profiled SCA Based on Random Convolution Kernels. *Information* **2025**, *16*, 351. [CrossRef]
18. Zhuang, F.; Qi, Z.; Duan, K.; Xi, D.; Zhu, Y.; Zhu, H.; Xiong, H.; He, Q. A comprehensive survey on transfer learning. *Proc. IEEE* **2020**, *109*, 43–76. [CrossRef]
19. Michele, C.; Oriol, M.; María, C.; Núria, D.; Bruno, C. Persistent Scatterer Interferometry: A review. *ISPRS J. Photogramm. Remote Sens.* **2016**, *115*, 78–89. [CrossRef]
20. Yang, G.; Wang, Z. A Deep Transfer Contrastive Learning Network for Few-Shot Hyperspectral Image Classification. *Remote Sens.* **2025**, *17*, 2800. [CrossRef]
21. Zhang, S.; Jafari, O.; Nagarkar, P. A Survey on Machine Learning Techniques for Auto Labeling of Video, Audio, and Text Data. *arXiv* **2021**. [CrossRef]
22. Nikolenko, S. *Synthetic Data for Deep Learning*; Springer: Cham, Switzerland, 2021. [CrossRef]
23. Qin, X.; Li, Q.; Ding, X.; Xie, L.; Wang, C.; Liao, M.; Zhang, L.; Zhang, B.; Xiong, S. A structure knowledge-synthetic aperture radar interferometry integration method for high-precision deformation monitoring and risk identification of sea-crossing bridges. *Int. J. Appl. Earth Obs. Geoinf.* **2021**, *103*, 102476. [CrossRef]
24. Yang, M.; Li, S.; Yu, H. A Transfer Learning Approach for Deformation Pattern Recognition in InSAR Time Series. *IEEE Trans. Geosci. Remote Sens.* **2025**, *63*. [CrossRef]
25. Berti, M.; Corsini, A.; Franceschini, S.; Iannacone, J.P. Automated classification of Persistent Scatterers Interferometry time series. *Nat. Hazards Earth Syst. Sci.* **2013**, *13*, 1945–1958. [CrossRef]

26. Selvakumaran, S.; Rossi, C.; Marinoni, A.; Webb, G.; Bennetts, J.; Barton, E.; Plank, S.; Middleton, C. Combined InSAR and Terrestrial Structural Monitoring of Bridges. *IEEE Trans. Geosci. Remote Sens.* **2020**, *58*, 7141–7153. [CrossRef]
27. Lea, C.; Flynn, M.D.; Vidal, R.; Reiter, A.; Hager, G.D. Temporal convolutional networks for action segmentation and detection. In Proceedings of the IEEE Conference on Computer Vision and Pattern Recognition, Honolulu, HI, USA, 21–26 July 2017; pp. 156–165. [CrossRef]
28. Vaswani, A.; Shazeer, N.; Parmar, N.; Uszkoreit, J.; Jones, L.; Gomez, A.N.; Kaiser, L.; Polosukhin, I. Attention is all you need. In Proceedings of the 31st International Conference on Neural Information Processing Systems, Long Beach, CA, USA, 4–9 December 2017; pp. 6000–6010. [CrossRef]
29. Lim, B.; Arık, S.Ö.; Loeff, N.; Pfister, T. Temporal fusion transformers for interpretable multi-horizon time series forecasting. *Int. J. Forecast.* **2021**, *37*, 1748–1764. [CrossRef]
30. Dempster, A.; Petitjean, F.; Webb, G.I. ROCKET: Exceptionally fast and accurate time series classification using random convolutional kernels. *Data Min. Knowl. Discov.* **2020**, *34*, 1454–1495. [CrossRef]
31. Huang, Q.; Monserrat, O.; Crosetto, M.; Crippa, B.; Wang, Y.; Jiang, J.; Ding, Y. Displacement Monitoring and Health Evaluation of Two Bridges Using Sentinel-1 SAR Images. *Remote Sens.* **2018**, *10*, 1714. [CrossRef]
32. Fuhrmann, T.; Garthwaite, M.C. Resolving Three-Dimensional Surface Motion with InSAR: Constraints from Multi-Geometry Data Fusion. *Remote Sens.* **2019**, *11*, 241. [CrossRef]

Disclaimer/Publisher's Note: The statements, opinions and data contained in all publications are solely those of the individual author(s) and contributor(s) and not of MDPI and/or the editor(s). MDPI and/or the editor(s) disclaim responsibility for any injury to people or property resulting from any ideas, methods, instructions or products referred to in the content.